Dalton Transactions

ROYAL SOCIETY OF CHEMISTRY

PAPER

View Article Online
View Journal | View Issue



Cite this: *Dalton Trans.*, 2026, **55**, 1164

# $SrMBe_2(BO_3)_2F_2$(M = Zn, Mg): two SBBO-like compounds obtained by cation regulation

Tong Wu, [a,b] Lei Kang, [a] Fan Liu,[a,b] Ruixin Guo,[c,d] Shu Guo, [c,d] Tianhong Huang,[a,b] Shuangyue Shang, [a,b] Lijuan Liu[a] and Xiaoyang Wang *[a]

Received 13th November 2025,
Accepted 15th December 2025

DOI: 10.1039/d5dt02730f

rsc.li/dalton

Cation regulation is a compelling strategy for developing new compounds with optimized crystal structures by atomic-scale manipulation. Herein, we report two new SBBO-like fluoroberyllium borates, $SrMgBe_2(BO_3)_2F_2$ (SMBBF) and $SrZnBe_2(BO_3)_2F_2$ (SZBBF). They crystallize in a trigonal system and feature a $[Be_3B_3O_6F_3]_\infty$ single layer stabilized by the incorporation of $Mg^{2+}/Zn^{2+}$ cations and $F^-$ cations. Both compounds exhibit deep-UV absorption edges below 200 nm. Theoretical calculations confirm their potential as deep-UV birefringent materials, with the corresponding birefringence values of 0.064 (SMBBF) and 0.063 (SZBBF) at 589 nm, respectively. This work demonstrates the effectiveness of cation regulation in designing novel borate-based optical materials.



## 1. Introduction

For decades, the rich structural diversity of borate frameworks has made them a fertile ground for discovering next-generation functional materials. Composed of flexible $[BO_3]^{3-}$ triangles and $[BO_4]^{5-}$ tetrahedra, borates exhibit a wide range of optical properties, such as second-harmonic generation, large birefringence, and photoluminescence.[1–4] The field of nonlinear optics is the area where borate compounds are most widely applied. Among the numerous nonlinear optical (NLO) borate crystals reported to date, β-$BaB_2O_4$ (BBO),[5] $LiB_3O_5$ (LBO),[6] $KBe_2BO_3F_2$ (KBBF),[7–9] and $Sr_2Be_2B_2O_7$ (SBBO)[10] stand out as prominent examples. BBO and LBO serve as workhorse materials for frequency conversion from the visible to the ultraviolet (UV) range, while KBBF is currently the only practical DUV NLO crystal. However, the KBBF crystal has a serious layer growth tendency which hinders the fabrication of bulk crystals with sufficient thickness for high-power laser applications. SBBO was once envisioned as a superior alternative to KBBF, yet the structural instability problem limits its applications in NLO.[11,12]

To overcome the structural instability problem, structural engineering strategies that chemically modify the coordination environment by cation regulation have proven particularly effective. Cation regulation in SBBO has led to an extended family of SBBO-type materials, such as $BaMBe_2(BO_3)_2F_2$ (M = Mg, Ca, Zn, Cd, Pb),[13–16] $Rb_3Al_3B_3O_{10}F$,[17] $MM'Be_2B_2O_6F$ (M = Na, M′ = Ca, Mg; M = K, M′ = Ca, Sr)[15,18] and $Rb_3Ba_3Li_2Al_4B_6O_{20}F$.[19] Notably, almost all these structural modifications exclude $Sr^{2+}$ from the lattice except $KSrBe_2B_2O_6F$, while the deliberate incorporation of foreign cations into the parent SBBO framework has not been widely studied.

In this work, we successfully incorporated divalent $Mg^{2+}$ and $Zn^{2+}$ directly into the SBBO structure, accompanied by the simultaneous introduction of fluoride ions, yielding two novel compounds: $SrMgBe_2(BO_3)_2F_2$ (SMBBF) and $SrZnBe_2(BO_3)_2F_2$ (SZBBF). The introduced cations effectively disrupt the original $[Be_3B_3O_6]_\infty$ bilayer, while fluoride ions stabilize a $[Be_3B_3O_6F_3]_\infty$ monolayer that preserves the essential structural features and moderate birefringence of the parent SBBO, suggesting their potential as deep-UV birefringent materials. The crystal structures and relevant physical properties of both compounds are systematically reported.

## 2. Experimental section

### 2.1 Synthesis and crystal growth

Single crystals of SMBBF and SZBBF were grown by spontaneous crystallization using a $NaBF_4$–$H_3BO_3$–NaF flux. The starting materials included $NaBF_4$ (Macklin Industrial Corp., 99.9%), NaF (Macklin, 99.9%), $H_3BO_3$ (Aladdin Industrial Corp., 99.9%), $SrF_2$ (Sinopharm Chemical Reagent Co., Ltd, 99.9%), MgO (Xilong Scientific, 99.9%), ZnO (Xilong Scientific, 99.9%), and BeO (99.9%). These reagents were mixed in a molar ratio

[a]*Beijing Center for Crystal Research and Development, Key Laboratory of Functional Crystals and Laser Technology, Technical Institute of Physics and Chemistry (TIPC), Chinese Academy of Sciences, Beijing 100190, China. E-mail: xywang@mail.ipc.ac.cn*
[b]*University of Chinese Academy of Sciences, Beijing 100049, China*
[c]*Shenzhen Institute for Quantum Science and Engineering, Southern University of Science and Technology, Shenzhen 518055, China*
[d]*International Quantum Academy, Shenzhen 518048, China*

of 1.5 : 4 : 2.5 : 1 : 1 ($NaBF_4$ : $H_3BO_3$ : NaF : $SrF_2$ : MgO/ZnO) and thoroughly ground in an agate mortar. Owing to the toxicity of BeO, all procedures were conducted in a ventilated workspace. The homogenized mixture was then transferred into a covered platinum crucible (40 mm in diameter) and heated in a box furnace to 800 °C, where it was held for 24 hours. Subsequently, the system was slowly cooled to 600 °C over 3 days, followed by further cooling to room temperature over an additional 2 days, yielding the final SMBBF and SZBBF crystals.

### 2.2 Powder X-ray diffraction (P-XRD) and structure determination

Powder X-ray diffraction (P-XRD) analyses of SMBBF and SZBBF samples were performed using a Bruker D8 powder X-ray diffractometer with Cu Kα radiation ($\lambda$ = 1.5418 Å) at room temperature. Data were collected with a scanning rate of 0.01 s per step and a step width of 0.02° per step over a 2theta range of 5° to 70°. The P-XRD patterns are presented in Fig. S1 and S2. Single crystal X-ray diffraction data for SMBBF and SZBBF were collected at 300 K using a Kappa Apex3 charge-coupled device diffractometer (Bruker) with graphite-monochromatic Mo Kα radiation ($\lambda$ = 0.71073 Å). Unit cell determination, data integration, and absorption correction were performed using the entire dataset. The raw data were corrected for background, polarization, and Lorentz factors using the APEX3 software, and multiscan absorption corrections were applied using the SADABS program package. The crystal structure was solved by direct methods and refined using the Olex2 program. The detailed crystallographic data are provided in Tables S1–S3.

### 2.3 Thermal analysis

The thermal properties of SMBBF and SZBBF were investigated by differential scanning calorimetry (DSC) using a Netzsch STA449F3 instrument. A sample weighing 15 mg was heated from 40 °C to 950 °C at a rate of 10 K $min^{-1}$, followed by cooling at the same rate.

### 2.4 UV-Vis-NIR diffuse reflectance spectroscopy

UV-Vis-NIR diffuse reflectance spectra of SMBBF and SZBBF powder were recorded in the range of 200–800 nm using a Cary 7000 UV-vis-NIR spectrophotometer. $BaSO_4$ was used as a reference.

### 2.5 Computational methods

First-principles calculations were performed using the plane-wave pseudopotential approach based on density functional theory (DFT), as implemented in CASTEP.[20,21] The ion–electron interactions were modeled using optimized norm-conserving pseudopotentials for all constituent elements.[22] The exchange–correlation energy was described by the Perdew–Burke–Ernzerhof (PBE) functional within the generalized-gradient approximation (GGA).[23] A kinetic energy cutoff of 940 eV was chosen with Monkhorst–Pack *k*-point meshes spanning less than 0.04 per $Å^3$ in the Brillouin zone.[24]

## 3. Results and discussion

### 3.1 Crystal structure

Using SBBO as a template, the replacement of the $Sr^{2+}$ ions between adjacent $[Be_3B_3O_6]_\infty$ bilayers with $Mg^{2+}$/$Zn^{2+}$ ions and the substitution of the intralayer $[BeO_4]$ groups with $[BeO_3F]$ groups led to the formation of SMBBF and SZBBF as shown in Fig. 1. SMBBF and SZBBF are isostructural and crystallize in the trigonal system with the space group $P\bar{3}$. Herein, the structure of SMBBF is discussed in detail as an example (Fig. 1b and c). In the asymmetric unit, all atoms (Sr, Mg, B, Be, O, and F) reside on crystallographically unique sites. Each B atom is coordinated by three O atoms, forming $[BO_3]$ triangles with B–O bond lengths of 1.3793(19) Å and O–B–O angles of 119.996(6)°. The Be atoms adopt a distorted $[BeO_3F]$ tetrahedral geometry, with Be–O and Be–F distances of 1.611(2) Å and 1.607(7) Å, respectively. These $[BeO_3F]$ tetrahedra connect with three adjacent $[BO_3]$ triangles *via* corner-sharing oxygen atoms, forming a two-dimensional $[Be_3B_3O_6F_3]_\infty$ layer extending in the *ab*-plane (Fig. 1b). Adjacent $[Be_3B_3O_6F_3]_\infty$ layers are alternately linked through Sr–F and Mg–O bonds. The Mg atoms are six-coordinated, forming $[MgO_6]$ polyhedra with Mg–O bond lengths of 2.0983(18) Å, while the Sr atoms are coordinated by six O and six F atoms, resulting in $[SrO_6F_6]$ polyhedra with Sr–O and Sr–F distances of 2.8582(19) Å and 2.6474(5) Å, respectively. Detailed crystallographic data are provided in Tables S1–S3. In SBBO, the intralayer spacing within the $[Be_3B_3O_6]_\infty$ bilayer is 3.92 Å, while the interlayer spacing between adjacent $[Be_3B_3O_6]_\infty$ bilayers is 3.74 Å. In SMBBF, these two values become 4.29 Å and 3.08 Å, respectively; in SZBBF, they are 4.29 Å and 3.10 Å, respectively. The increase in intralayer spacing from 3.92 Å to 4.29 Å can be attributed to the change in intralayer connectivity from Be–O–Be covalent bonds in SBBO to F–Sr–F ionic bonds in SMBBF/SZBBF. This structural alteration not only increases the number of atoms within the layer but also weakens the bonding character from covalent to ionic, both contributing to the expanded intralayer

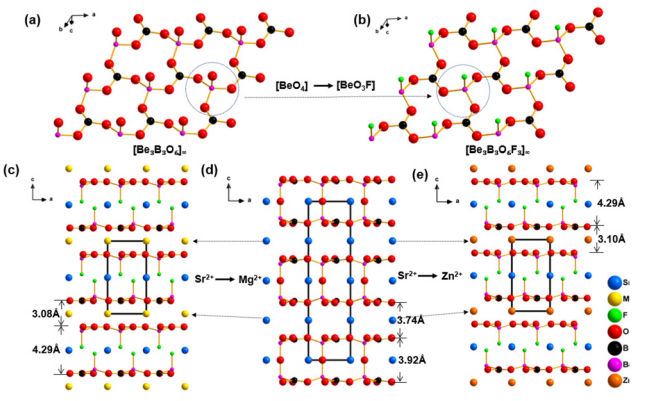


Fig. 1 Structural evolution from SBBO to SMBBF and SZBBF. (a) $[Be_3B_3O_6]_\infty$ layer in SBBO, (b) $[Be_3B_3O_6F_3]_\infty$ layer in SMBBF, (c) crystal structure of SMBBF, (d) crystal structure of SBBO, and (e) crystal structure of SZBBF.

spacing. Conversely, the decrease in interlayer spacing from 3.74 Å to 3.08/3.10 Å arises from the replacement of $Sr^{2+}$ by the much smaller $Mg^{2+}/Zn^{2+}$ cations in the interlayer region, whose reduced ionic radii directly compress the interlayer distance. Bond valence sum calculations for Sr, Be, Mg, B, O, and F confirm oxidation states of +2, +2, +2, +3, −2, and −1, respectively (Table S3). The consistency between bond lengths and bond valence sums supports the structural model and indicates the absence of significant internal strain in both SMBBF and SZBBF.

### 3.2 UV-vis diffuse reflectance spectroscopy

The ultraviolet–visible reflectance spectra of SMBBF and SZBBF are presented in Fig. 2. The spectra demonstrate high diffuse reflectance values of more than 90% across the visible spectral region for both SMBBF and SZBBF. For SMBBF, the reflectance begins to decrease below 400 nm due to some extrinsic absorption with a residual reflectance of 80% at 200 nm, while that of SZBBF is less than 60% at 200 nm. These results suggest that the absorption edges of SMBBF and SZBBF lie below 200 nm. It should be noted that unintended absorption features are observed in the 200–400 nm range. We attribute these features to the presence of potential impurity ions, such as $Fe^{3+}$ (4.8 eV, ~258 nm), $Cr^{3+}$ (3.1 eV, ~400 nm) and $Mn^{4+}$ (6.0 eV, ~207 nm), which are known to introduce absorption bands in this region.[25,26] Nevertheless, our results remain meaningful: even with these impurity-related absorptions, the diffuse reflectance spectra still show reflectance values greater than 45% within the 200–300 nm range.

### 3.3 Thermal analysis

The thermal behaviors of SMBBF and SZBBF were investigated by thermogravimetry–differential scanning calorimetry (TG-DSC), as shown in Fig. 3. For SMBBF, a sharp endothermic peak appears at 864 °C on the heating curve, accompanied by an exothermic peak at 760 °C on the cooling curve. A thermal hysteresis of more than 100 °C between the two peaks, together with observable mass loss, suggests that the thermal

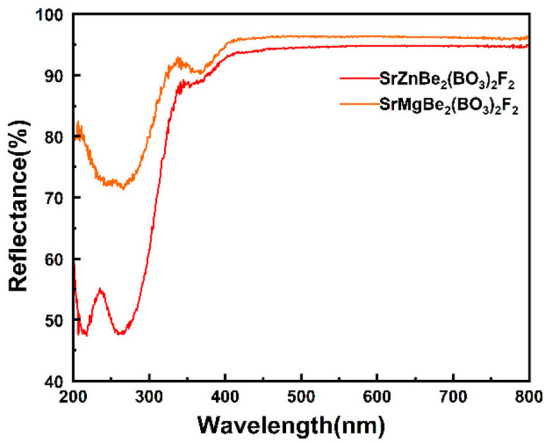


Fig. 2 UV–Vis reflectance spectra of SMBBF and SZBBF.

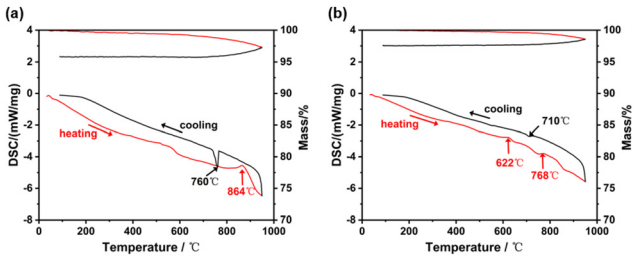


Fig. 3 TG-DSC curves of SMBBF (a) and SZBBF (b).

event at 864 °C corresponds to decomposition rather than melting. In the case of SZBBF, two small endothermic peaks are observed at 622 °C and 768 °C during heating, while the cooling curve displays a small exothermic peak near 710 °C. Combined with the overall mass loss, this also indicates a decomposition process occurring at both temperatures. Powder X-ray diffraction (PXRD) was performed on the residues obtained after melting as shown in Fig. S3 and S4. The resulting patterns displayed numerous small, disordered peaks, which could not be identified through pattern matching. These results confirm that both SMBBF and SZBBF are incongruent-melting compounds.

### 3.4 Calculation results

To elucidate the structure–property relationships in SMBBF and SZBBF, we computed their refractive indices, bandgaps, and partial densities of states (PDOS). All calculations were performed within the scissors-corrected GGA-PBE framework,[27,28] using a scissor operator of 2.0 eV, the same as that of $Sr_2Be_2B_2O_7$. The same scissor value was applied to both compounds due to their similar elemental composition and structural features to SBBO. SZBBF exhibits an indirect bandgap, whereas SMBBF shows a direct bandgap. The calculated bandgaps increase from 4.517 eV for SZBBF to 5.707 eV for SMBBF (Fig. 4a and c). Notably, replacing Zn with Mg leads to a widening of the bandgap and a corresponding blue shift in the ultraviolet absorption edge.

As shown in Fig. 4b and d, the PDOS profiles reveal distinct electronic contributions near the band edges. In SMBBF, the valence band maximum (VBM) is dominated by O 2p, B 2p, Be 2p, and Mg 2p orbitals, while in SZBBF, it consists mainly of O 2p, B 2p, Be 2p, and Zn 3d orbitals. In the lower conduction band region (0–6 eV for SMBBF, 0–5 eV for SZBBF), SMBBF is primarily composed of Mg 2p, B 2p, and Be 2p orbitals, whereas SZBBF features B 2p, Be 2p, and Zn 4s orbitals. These differences in conduction band composition account for the larger calculated bandgap of SMBBF compared to SZBBF.

The refractive indices of both compounds, derived from the dielectric function $\varepsilon(\omega) = \varepsilon1(\omega) + i\varepsilon2(\omega)$, are presented in Fig. 5. The imaginary part $\varepsilon2(\omega)$ was computed first, followed by the real part $\varepsilon1(\omega)$ *via* the Kramers–Kronig relation; the refractive indices were then obtained from $\varepsilon1(\omega)$. Both crystals exhibit strong optical anisotropy with $n_o < n_e$, confirming them as negative uniaxial crystals. The calculated birefringence values

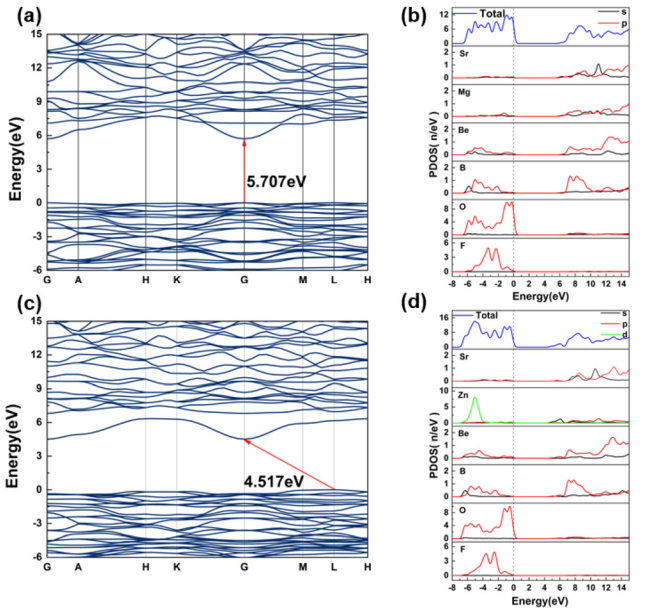


Fig. 4 Partial DOS of SMBBF (b) and SZBBF (d); and calculated band structures of SMBBF (a) and SZBBF (c).

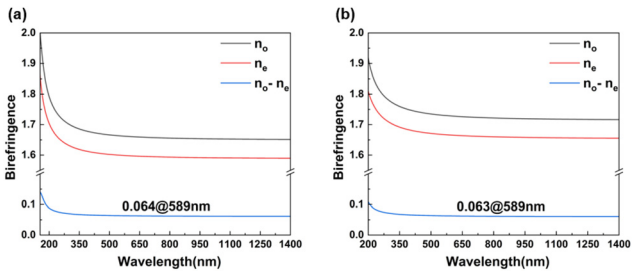


Fig. 5 Calculated refractive indices of SMBBF (a) and SZBBF (b).

at 589 nm are 0.064 for SMBBF and 0.063 for SZBBF. As summarized in Table 1, both compounds exhibit birefringence values comparable to those of other reported SBBO-type materials. Together with their short ultraviolet absorption edges (below 200 nm), these results indicate that SMBBF and SZBBF are promising birefringent crystals for the deep-ultraviolet (DUV) spectral region.

Table 1 Structures and birefringence values of SBBO-type beryllium borates

| Compound | Symmetry | $\lambda_{cutoff}$ (nm) | Birefringence |
|---|---|---|---|
| $Sr_2Be_2B_2O_7$ [10] | $P\bar{6}c2$ | 165 | 0.062 (1064 nm)[c] |
| $NaMgBe_2(BO_3)_2F$ [15] | $P\bar{3}c1$ | <195 | 0.081 (546 nm)[c] |
| $NaCaBe_2(BO_3)_2F$ [18] | $Cc$ | 190 | 0.076 (589 nm)[b] |
| $KCaBe_2(BO_3)_2F$ [18] | $P\bar{3}c1$ | — | — |
| $KSrBe_2(BO_3)_2F$ [18] | $P6_3/m$ | — | — |
| $BaMgBe_2(BO_3)_2F_2$ [16] | $P\bar{3}c1$ | <185 | 0.064 (589 nm)[b] |
| $BaCaBe_2(BO_3)_2F_2$ [16] | $P\bar{3}c1$ | <185 | 0.063 (589 nm)[b] |
| $BaZnBe_2(BO_3)_2F_2$ [14] | $P\bar{3}c1$ | 300 | 0.061 (589 nm)[b] |
| $BaCdBe_2(BO_3)_2F_2$ [15] | $P\bar{3}c1$ | <190 | 0.059 (546 nm)[c] |
| $BaPbBe_2(BO_3)_2F_2$ [13] | $P\bar{3}m1$ | 279 | 0.054 (564 nm)[c] |
| $SrMgBe_2(BO_3)_2F_2$ [a] | $P\bar{3}$ | <200 | 0.064 (589 nm)[b] |
| $SrZnBe_2(BO_3)_2F_2$ [a] | $P\bar{3}$ | <200 | 0.063 (589 nm)[b] |

[a] This work. [b] Calculated results. [c] Experimental results.

## 4. Conclusion

In summary, two new fluoroberyllium borates, $SrMgBe_2(BO_3)_2F_2$ (SMBBF) and $SrZnBe_2(BO_3)_2F_2$ (SZBBF), have been successfully synthesized. Both compounds exhibit a deep-UV absorption edge below 200 nm. Theoretical calculations reveal birefringence values ($\Delta n$ at 589 nm) of 0.064 for SMBBF and 0.063 for SZBBF, with the corresponding band gaps of 5.707 eV and 4.517 eV, respectively. These properties confirm the potential of SMBBF and SZBBF as deep-UV birefringent materials. Further work on the growth and characterization of large single crystals is currently underway. Moreover, this study demonstrates that structural optimization through rational cation substitution provides an effective strategy for designing high-performance deep-UV birefringent and potentially other functional optical materials.

## Conflicts of interest

There are no conflicts to declare.

## Data availability

The data supporting the findings of this study are available within the article and its supplementary information (SI). Supplementary information: P-XRD patterns, crystal data and structural refinement, selected bond lengths and bond angles, atomic coordinates and equivalent isotropic displacement parameters. See DOI: https://doi.org/10.1039/d5dt02730f.

CCDC 2500203 and 2500237 contain the supplementary crystallographic data for this paper.[29a,b]

## Acknowledgements

This work is supported by grants from the National Natural Science Foundation of China (52272012). Shu Guo acknowledge the financial support from the National Natural Science Foundation of China (22205091), the Guangdong Pearl River Talent Plan (2023QN10C793).

## References

1 C. T. Chen, L. Bai, Z. Z. Wang and R. K. Li, *J. Cryst. Growth*, 2006, **292**, 169–178.
2 M. Mutailipu, K. R. Poeppelmeier and S. Pan, *Chem. Rev.*, 2021, **121**, 1130–1202.
3 B. Dalai and S. K. Dash, *Opt. Mater.*, 2023, **143**, 113909.
4 W. Yao, R. He, X. Wang, Z. Lin and C. Chen, *Adv. Opt. Mater.*, 2014, **2**, 411–417.

5 C. T. Chen, B. C. Wu, A. D. Jiang and G. M. You, *Sci. Sin., Ser. B*, 1985, **28**, 235–243.
6 C. T. Chen, Y. C. Wu, A. D. Jiang, B. C. Wu, G. M. You, R. K. Li and Z. S. Lin, *J. Opt. Soc. Am. B*, 1989, **6**, 616–621.
7 C. Chen, Z. Xu, D. Deng, J. Zhang, G. K. L. Wong, B. Wu, N. Ye and D. Tang, *Appl. Phys. Lett.*, 1996, **68**, 2930–2932.
8 L. Liu, L. Zhao, X. Zhou and X. Wang, *Appl. Phys. B*, 2022, **128**, 17.
9 C. T. Chen, G. L. Wang, X. Y. Wang and Z. Y. Xu, *Appl. Phys. B*, 2009, **97**, 9–25.
10 C. T. Chen, Y. B. Wang, B. C. Wu, K. C. Wu, W. L. Zeng and L. H. Yu, *Nature*, 1995, **373**, 322–324.
11 X. Cheng, Y. Zhang, L. Liu, X. Wang, M.-H. Whangbo, J. Lin and S. Deng, *J. Phys. Chem. Lett.*, 2021, **12**, 11399–11405.
12 X. Y. Meng, X. H. Wen and G. L. Liu, *J. Korean Phys. Soc.*, 2008, **52**, 1277–1280.
13 R. Guo, S. Guo, M. Xia, L. Liu, M. Li, S. Zhao and X. Wang, *Inorg. Chem.*, 2023, **62**, 3860–3865.
14 R. Guo, X. Liu, C. Tao, C. Tang, M. Xia, L. Liu, Z. Lin and X. Wang, *Dalton Trans.*, 2021, **50**, 2138–2142.
15 R. Guo, X. Jiang, S. Guo, M. Xia, L. Liu, Z. Lin and X. Wang, *Inorg. Chem.*, 2022, **61**, 7624–7630.
16 S. Guo, X. Jiang, M. Xia, L. Liu, Z. Fang, Q. Huang, R. Wu, X. Wang, Z. Lin and C. Chen, *Inorg. Chem.*, 2017, **56**, 11451–11454.
17 S. Zhao, P. Gong, S. Luo, S. Liu, L. Li, M. A. Asghar, T. Khan, M. Hong, Z. Lin and J. Luo, *J. Am. Chem. Soc.*, 2015, **137**, 2207–2210.
18 H. Huang, J. Yao, Z. Lin, X. Wang, R. He, W. Yao, N. Zhai and C. Chen, *Chem. Mater.*, 2011, **23**, 5457–5463.
19 H. Yu, J. Young, H. Wu, W. Zhang, J. M. Rondinelli and S. Halasyamani, *Adv. Opt. Mater.*, 2017, **5**, 1700840.
20 M. C. Payne, M. P. Teter, D. C. Allan, T. A. Arias and J. D. Joannopoulos, *Rev. Mod. Phys.*, 1992, **64**, 1045–1097.
21 S. J. Clark, M. D. Segall, C. J. Pickard, P. J. Hasnip, M. I. J. Probert, K. Refson and M. C. Payne, *Z. Kristallogr. – Cryst. Mater.*, 2005, **220**, 567–570.
22 J. S. Lin, A. Qteish, M. C. Payne and V. Heine, *Phys. Rev. B: Condens. Matter Mater. Phys.*, 1993, **47**, 4174–4180.
23 J. P. Perdew, K. Burke and M. Ernzerhof, *Phys. Rev. Lett.*, 1996, **77**, 3865–3868.
24 D. J. Chadi, *Phys. Rev. B*, 1977, **16**, 1746–1747.
25 L. Liu, C. Liu, X. Wang, Z. G. Hu, R. K. Li and C. T. Chen, *Solid State Sci.*, 2009, **11**, 841–844.
26 M. E. Innocenzi, R. T. Swimm, M. Bass, R. H. French, A. B. Villaverde and M. R. Kokta, *J. Appl. Phys.*, 1990, **67**, 7542–7546.
27 J. Lin, M.-H. Lee, Z.-P. Liu, C. T. Chen and C. J. Pickard, *Phys. Rev. B:Condens. Matter Mater. Phys.*, 1999, **60**, 13380–13389.
28 L. Kang, F. Liang, X. Jiang, Z. Lin and C. Chen, *Acc. Chem. Res.*, 2020, **20**(53), 209–217.
29 (*a*) CCDC 2500203: Experimental Crystal Structure Determination, 2025, DOI: 10.5517/ccdc.csd.cc2pxnq0; (*b*) CCDC 2500237: Experimental Crystal Structure Determination, 2025, DOI: 10.5517/ccdc.csd.cc2pxpt4.